

**1 Estimating profiles of dissipation rate in the upper ocean from acoustic
2 Doppler measurements below surface following platforms**

3 Kristin Zeiden,¹ Jim Thomson,¹ and James Girton,¹

4 *¹ Applied Physics Laboratory, University of Washington, Seattle WA*

5 Corresponding author: Kristin Zeiden, kzeiden@uw.edu

6 ABSTRACT: High resolution profiles of vertical velocity obtained from two different surface-
7 following autonomous platforms, Surface Wave Instrument Floats with Tracking (SWIFTs) and
8 a Liquid Robotics SV3 Wave Glider, are used to compute dissipation rate profiles $\epsilon(z)$ between
9 0.5 and 5 m depth via the structure function method. The main contribution of this work is to
10 update previous SWIFT methods (Thomson 2012) to account for bias due to surface gravity waves,
11 which are ubiquitous in the near-surface region. We build upon previous work to remove wave bias
12 in which analytic modifications are made to the structure function model (Scannell et al. 2017).
13 However, we find the analytic approach to be insufficient in this application due a limitation on
14 integration ranges imposed by strong vertical gradients in $\epsilon(z)$ near the surface. As an alternative,
15 we pre-filter the data by removing profiles of wave orbital velocities obtained from empirical
16 orthogonal functions (EOFs) of the data prior to computing the structure function. The strength
17 of the EOF filtering technique is that it does not require any assumptions about the structure of
18 non-turbulent shear, and does not add any additional degrees of freedom in the least-squares fit to
19 the model of the structure function. In comparison to the analytic method, $\epsilon(z)$ estimates obtained
20 via empirical filtering have substantially reduced noise and clearer dependence on near-surface
21 wind speed.

22 **1. Introduction**

23 Turbulence in the ocean surface boundary layer modulates the exchange of heat, momentum and
24 gases between the ocean and atmosphere. Thus our understanding of the chemical and energy
25 balance across the air-sea interface is predicated on a careful accounting of turbulent dissipation
26 rate, $\epsilon(z)$, in the upper ocean (Belcher et al. 2012). While $\epsilon(z)$ often obeys classic ‘law of the wall’
27 boundary layer scaling within the mixed layer under steady wind forcing conditions (i.e. $\epsilon(z) \propto z^{-1}$),
28 energetic surface processes such as wave breaking, Langmuir turbulence and convective overturns
29 can lead to strong near-surface (upper 1-10 meters) enhancement and intermittency which is
30 difficult to predict (Terray et al. 1996; Gerbi et al. 2009; Thomson et al. 2016). Other processes
31 can suppress near-surface mixing, such as diurnal surface heating (Sutherland and Melville 2015).
32 An added difficulty lies in referencing stationary measurements to a moving sea-surface (Thomson
33 et al. 2016). Recent advances in the application of autonomous surface-following platforms have
34 shown them to be a promising tool for measuring $\epsilon(z)$ in the very near surface under a wide
35 range of forcing conditions (e.g. Thomson 2012; Grare et al. 2018; Hughes et al. 2021). However,
36 instrument motion and strong wave orbital velocities often make it difficult to isolate turbulence
37 in the surface following reference frame. To that end, this manuscript provides an update to the
38 methodology employed by Thomson (2012) to estimate $\epsilon(z)$ from high-resolution (HR) acoustic
39 doppler current profiler (ADCP) data obtained with Surface Wave Instrument Floats with Tracking
40 (SWIFTs). We seek to remove previously unaccounted for bias in the estimate of $\epsilon(z)$ due to
41 platform motion and waves, as well as expand the application of our methodology to ADCP data
42 collected from a Liquid Robotics SV3 Wave Glider (Thomson et al. 2018).

43 Estimates of dissipation rate have commonly been derived from ADCP data using Fourier analysis
44 of high frequency velocity time series due to past difficulty in achieving high spatial resolution
45 measurements. That method requires the assumption of a steady background velocity which moves
46 isotropic turbulence past the instrument, thereby converting time series to spatial-series (the well
47 known ‘frozen-field’ assumption). An advective velocity is particularly difficult to define in the
48 near surface due to the presence of surface waves, strong wind driven shear and other energetic
49 surface currents. Recent advancements in the application of pulse-to-pulse coherent methods of
50 measuring velocity with ADCPs have enabled high spatial resolution velocity measurements (‘HR’
51 mode, Shcherbina et al. 2018), which can be used to estimate dissipation rate without needing to

52 define an advective velocity (Gargett 1999). This is particularly advantageous for application to
53 Lagrangian platforms, which are subject to significant wave-induced motion with respect to the
54 water (Zippel et al. 2018).

55 Here we follow the structure function method (SF method) of Wiles et al. (2006), which treats
56 individual profiles of velocity as independent realizations of the spatial structure of turbulence, with
57 no coherent relation to the profile observed before or after. The method consists of least-squares
58 fitting (LSF) the second order velocity structure function $D(r)$ to a theoretical model derived from
59 Taylor and Kolmogorov scaling theories, $D(r) \propto \epsilon r^{2/3}$. The model is assumed to be valid over
60 some limited range of scales r within the inertial subrange. The SF method has typically been
61 applied to velocity data obtained with bottom mounted and moored ADCPs (e.g. Mohrholz et al.
62 2008; Lucas et al. 2014; Sutherland and Melville 2015; McMillan et al. 2016; Scannell et al. 2017),
63 while applications in the very near surface have been rarer. Gemmrich (2010) estimated $\epsilon(z)$ in the
64 surface 1 m by applying the SF method to ADCP data collected from a ship-mounted frame. More
65 recently, Thomson (2012), Thomson et al. (2016) and Zippel et al. (2018) used the SF method
66 to estimate $\epsilon(z)$ in the surface 0.5 m from upward looking pulse-coherent ADCPs mounted on
67 SWIFT drifters.

68 The inherent challenge of the SF method is to isolate turbulence from non-turbulent velocities.
69 Unlike Fourier spectral methods, which differentiate between these signals in frequency and
70 wavenumber space, non-turbulent velocity gradients contribute to $D(r)$ at each scale. In the upper
71 ocean, surface gravity waves are the most common source of bias. Recently, Scannell et al. (2017)
72 introduced an analytic modification to the model of the inertial subrange structure function to
73 account for wave bias. The authors demonstrated that the wave contribution goes as r^2 , and can
74 theoretically be separated from the turbulent component by introducing a third term in the model
75 proportional to r^2 . They validated this modified SF method using velocity data collected with
76 ADCPs moored at ~ 20 , 30 and 50 m depth, well outside the region of active wave breaking.
77 No estimates were made close to the surface because the broadband ADCPs lacked the necessary
78 resolution and their uplooking configuration caused strong acoustic reflections in the shallowest
79 bins. The authors integrated over each 3-m profile to produce timeseries of ϵ at each ADCP depth.
80 In the near surface, we are interested in resolving vertical structure as $\epsilon(z)$ can vary many orders
81 of magnitude over a few meters (Thomson et al. 2016). Previous studies utilizing the SF method

to estimate $\epsilon(z)$ in using SWIFT drifters did not attempt to correct for bias due to surface waves (Thomson 2012; Thomson et al. 2016; Zippel et al. 2018). Zippel et al. (2018) used cross-spectra between velocity data and an onboard IMU to remove bias due to platform motion. However, the platform motion turns out to be a secondary concern in the SF method as the motion mostly affects time-domain calculations.

In this manuscript we present updates to the methodology used by Thomson (2012), Thomson et al. (2016) and Zippel et al. (2018) to compute dissipation from pulse-coherent high-resolution (HR) ADCP data obtained in the near surface with SWIFT drifters. We refine the structure function algorithm, introduce a new method to account for bias due to non-turbulent shear, and expand the application to data collected with a surface following SV3 Wave Glider. In contrast to previous SWIFT studies, the data used here are in a downward looking orientation and span \sim 0.5-5 m depth. The increased profile range enables a clear picture of the impact of wave bias on the structure function in close proximity to the surface. Our updated methodology builds upon the method introduced by Scannell et al. (2017) to account for wave bias, however we explore an alternative in which low-mode wave profiles computed from empirical orthogonal functions (EOFs) of the data are removed prior to computing the structure functions. This new approach is motivated by the limited spatial integration ranges necessitated by our desire to resolve the vertical structure of dissipation rate, which has the effect of limiting the number of points included in the least-squares fit. Our results indicate that the empirical method of isolating turbulent velocity produces similar results to the analytic method introduced by Scannell et al. (2017), but with significantly reduced noise and lower mean-square percent error between the model and the data. Most importantly, these new dissipation estimates exhibit a clear dependence on near-surface wind speed over the broader SWIFT and Wave Glider datasets. This effect is heavily obscured by noise in the estimate obtained via the analytically modified SF method.

We begin with an overview of the inertial subrange structure function theory in section 2, followed by a description of the data in section 3. In section 4, we give a detailed examination of velocity data from a single burst obtained during the SWIFT mission and subsequent dissipation estimates from that burst. In section 5, we apply the refined methodology to the broader mission data from both platforms and discuss the results.

111 **2. Theory**

112 In the absence of analytic descriptions of turbulence, oceanographers presently rely on a statistical
113 model put forward by Taylor (1937) and Kolmogorov (1941). This model is predicated on the
114 existence of an “inertial subrange” in which the rate of kinetic energy transfer between different
115 scales of motion (ϵ) is a constant independent of scale and viscosity. From this assumption,
116 Taylor used dimensional analysis to argue $\epsilon \propto u(r)^3 r^{-1}$ in the inertial subrange, where $u(r)$ is the
117 characteristic velocity of turbulent eddies at scale r .

118 The method used to estimate $\epsilon(z)$ in this study relates Taylor’s theoretical scaling to measurements
119 of the second order velocity structure function, $D(z, r) = \langle [u(z - \frac{r}{2}) - u(z + \frac{r}{2})]^2 \rangle$, i.e. the ensemble-
120 average squared velocity difference over a separation scale r centered at vertical position z . If the
121 energy at depth z and scale r is predominately due to turbulent eddies, Taylor’s scaling suggests

$$D(z, r) = C_v^2 \epsilon(z)^{2/3} r^{2/3} \quad (1)$$

122 Here C_v^2 is a constant empirically determined to be ~ 2.1 (Wiles et al. 2006). Dissipation rate can
123 then be estimated by least-squares fitting the observed velocity structure function at each depth to
124 a linear function of the form

$$D(r) = Ar^{2/3} + N \quad (2)$$

125 and taking $\epsilon(z) = (A(z)/C_v^2)^{3/2}$. The model intercept N gives the uncertainty in u^2 , assumed to be
126 proportional to the instrument noise at each depth.

127 This model of inertial subrange turbulence holds approximately in the deep ocean away from
128 boundaries and in the presence a steady mean flow, but near the surface there are likely high-
129 frequency, non-turbulent velocity gradients which contribute to D . The most likely source of bias
130 is energetic surface gravity waves with small vertical decay scales (i.e. short waves). Waves may
131 also indirectly contribute to bias if the wave-induced platform motion is significant in the presence
132 of otherwise steady background shear. Scannell et al. (2017) recently developed an analytic
133 framework to account for wave bias in $D(r)$: if non-turbulent velocity gradients are sufficiently
134 linear on the spatial scales of interest, their contribution to the structure function will go as
135 r^2 . This modified model of the structure function accounts for both turbulent and non-turbulent

136 contributions by the addition of a third term:

$$D(r) = Ar^{2/3} + B(r^{2/3})^3 + N \quad (3)$$

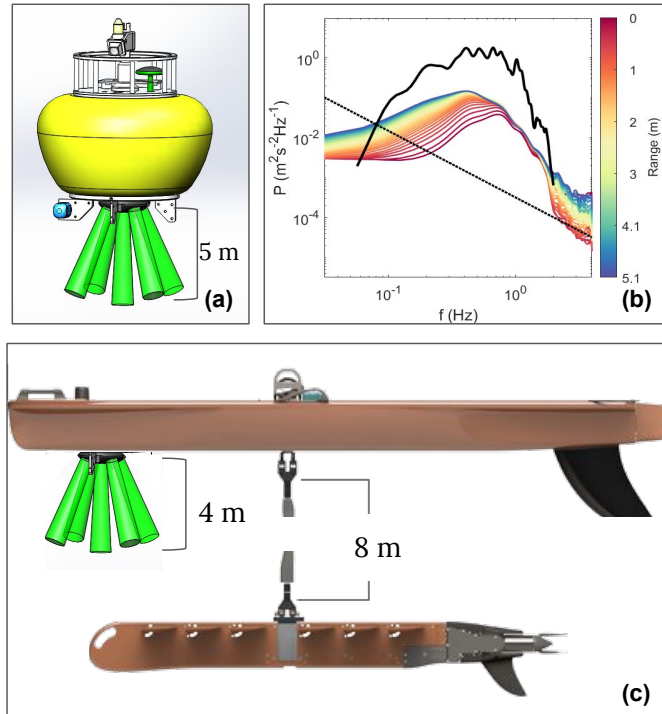
137 The original relationship between ϵ and A is preserved, and $\epsilon(z)$ may be determined in the same
138 fashion by fitting the observed $D(r)$ to Eq. 3 at each depth.

139 3. Dataset Description

140 To demonstrate the robustness of the SF method of estimating turbulence from ADCP data
141 collected in a surface following reference frame, we apply the method to data obtained with two
142 different platforms; Surface Wave Instrument Floats with Tracking (SWIFTs, Thomson 2012) and
143 a Liquid Robotics SV3 Wave Glider (Hine et al. 2009; Thomson et al. 2018). The SWIFTs and
144 Wave Glider were equipped with the same ADCPs (Nortek Signature 1000), but operated under
145 very different environmental conditions. The SWIFTs were deployed in the Southern California
146 Bight in late March 2017 during the Office of Naval Research ‘Langmuir Circulation’ Departmental
147 Research Initiative (LC-DRI) field experiment. The Wave Glider was deployed in the Southern
148 Ocean in November 2019 during a 4-month survey of the Antarctic Circumpolar Current fronts
149 within Drake Passage. We apply our methodology to subsets of the data collected away from strong
150 fronts and during periods with near-surface wind speeds less than 15 ms^{-1} , such that we expect
151 dissipation rates to be primarily a function of wind speed.

152 a. ADCP configuration

160 The Nortek Signature 1000 has four slanted beams operating in broadband mode, and a fifth
161 vertical beam which operates in an interleaving pulse-coherent high-resolution (HR) mode (Figure
162 1a,c). In HR mode, a pair of coherent short pulses separated by a lag time much longer than the
163 pulse duration is emitted each ping (a ‘pulse-pair’). Along-beam velocity is then a function of
164 the phase of the complex correlation of the pulse-pair echo, lag time, the carrier frequency of the
165 pulses, and the local sound speed (Eq. 1 in Shcherbina et al. 2018). Although the precise temporal
166 and spatial resolution is user defined, HR mode is designed to produce profiles of along-beam
167 velocity with bin sizes of a few centimeters at frequencies greater than 1 Hz. For this study,
168 ADCPs on both platforms were configured to sample in 0.04 m bins at 8 Hz over 8-minute “bursts”



153 FIG. 1. Instrument schematics for the (a) SWIFT drifters, as well
 154 as (b) along-beam velocity frequency spectra computed from a single 8-minute burst of data obtained from a
 155 SWIFT mounted Signature 1000 ADCP. The profile ranges were 5.12 m and 3.84 m on the SWIFT and SV3,
 156 respectively. ADCP depth bins were 0.04 m on both platforms. Frequency spectra in (b) are colored by range
 157 from the transducer (red colors are closer), and the black line shows vertical velocity of the instrument obtained
 158 from the onboard inertial motion unit. Velocity variance at all depths is dominated by a broadband peak around
 159 0.5 Hz due to surface gravity waves.

169 (Table 1). The range of the center beam in HR mode was 5.12 m as configured on the SWIFTS, and
 170 3.84 m on the Wave Glider. The depth of the transducer on both platforms was 0.2 m. Combined
 171 with a blanking distance of 0.1 m, the effective depth ranges of the ADCPs were 0.3 m to 5.42 m
 172 and 4.14 m on the SWIFTS and Wave Glider, respectively. The ADCPs onboard the SWIFTS were
 173 configured to burst-sample every 12 minutes. The ADCP onboard the Wave Glider was configured
 174 to burst-sample at the top of every hour.

175 Prior to analysis, velocity data were quality controlled by removing velocity spikes which occur
 176 due to phase ambiguity inherent in the pulse-pair coherence method of determining velocity

Signature 1000 Burst Sampling Configurations					
Platform	Bin Size	Range	Depth	Rate	Duration
SWIFT	0.04 m	5.12 m	0.2 m	8 Hz	8 min
Wave Glider	0.04 m	3.84 m	0.2 m	8 Hz	8 min

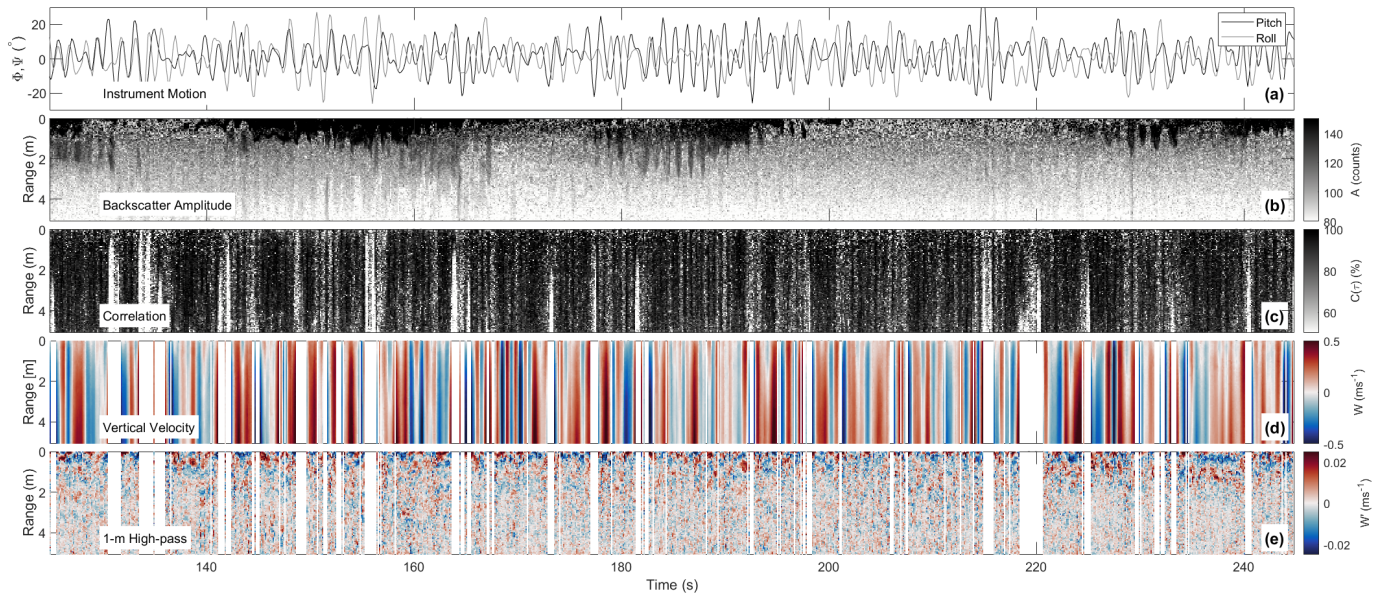
TABLE 1. ADCP configurations as deployed on the SWIFTs and Liquid Robotics SV3 Wave Glider.

(Shcherbina et al. 2018). Spikes are identified in each ping using a threshold maximum deviance from a 1-m median filtered profile, and comprise anywhere from 10 - 80% of the data depending on the environmental conditions (i.e. high or low scattering environments). In addition to removing individual data spikes, entire pings are removed if the standard deviation of the filtered velocity profile exceeds 0.01 ms^{-1} , typically a symptom of excessive spiking. Additional details of the de-spiking routine are given in the Appendix.

b. Example Data

An example two minutes of quality controlled ADCP data from a single 8 minute burst obtained from a SWIFT drifter is given in Figure 2. Instrument orientation (pitch and roll), acoustic backscatter amplitude and pulse-pair correlation are shown in addition to the along-beam velocity. The tilt of the instrument varies up to 30 degrees, but with a standard deviation angle from the vertical of just 10 degrees (Fig. 2a). Corresponding vertical displacements are 1 m at the base of the profile, though we note this does not affect the along-beam bin spacing. Acoustic back-scatter amplitude is highest near the transducer and characterized by strong intermittency every $\sim 20\text{-}30$ seconds (Fig. 2b). Weaker pulses in amplitude with a period of about 1 second are due to the SWIFT bobbing at its natural frequency. Pulse-pair echo correlation is 85% on average, but randomly drops below 50% over an entire profile (Fig. 2c). Pings with correlation drop-out are typically characterized by a high percentage of data spikes and are discarded in our de-spiking routine (Appendix). In this example 10% of all pings in the burst are discarded. Along-beam velocity is $O(0.1 \text{ ms}^{-1})$ due to a combination of waves and instrument bobbing (Fig. 2d). However, a simple 1-m moving Hanning window filter applied to each velocity profile reveals clear fine-scale structure in the data (Fig. 2e). The high-passed velocity is $O(0.01 \text{ ms}^{-1})$, an order of magnitude weaker than the ambient waves.

Velocity spectra computed from the example burst data are dominated by waves and platform motion at all frequencies (Fig. 1c). Spectra are plotted as a function of range from the transducer (colored lines). Overlaid in black is the spectrum of vertical instrument velocity obtained from



184 Fig. 2. Example ADCP data collected from a SWIFT drifter. Shown are (a) instrument pitch and roll,
 185 (b) back-scatter amplitude, (c) pulse-pair correlation, (d) along-beam velocity and (e) 1-m high passed along-beam
 186 velocity. The velocity data have been de-spiked (Appendix). Surface gravity waves and the bobbing of the
 187 SWIFT at its natural frequency dominate the along-beam velocity variance, but fine-scale structure is evident in
 188 the high-passed data. Only two minutes of the 8-minute burst are shown here for clarity.

207 an onboard inertial motion unit (i.e. platform motion spectra). The spectra are dominated by a
 208 broadband peak from 0.1 - 1 Hz due to surface gravity waves. Energy at all frequencies increases
 209 with distance from the transducer due to the wave shear, except near 1 Hz due to the bobbing of
 210 the SWIFT. Vertical platform motion with respect to the water (i.e. bobbing) introduces a relative
 211 velocity independent of distance from the transducer. We note that using frequency spectra to
 212 estimate dissipation in this application would require both the removal of wave velocities from the
 213 data and an accurate characterization of an advective velocity for each depth bin. However, even if
 214 wave velocities could be fully characterized, the ping-to-ping horizontal and vertical displacement
 215 of each ADCP bin due to the strong platform motion (up to 1 m at the base of the profile) likely
 216 violates the coherence of the turbulent velocity observations in time. This motivates treating

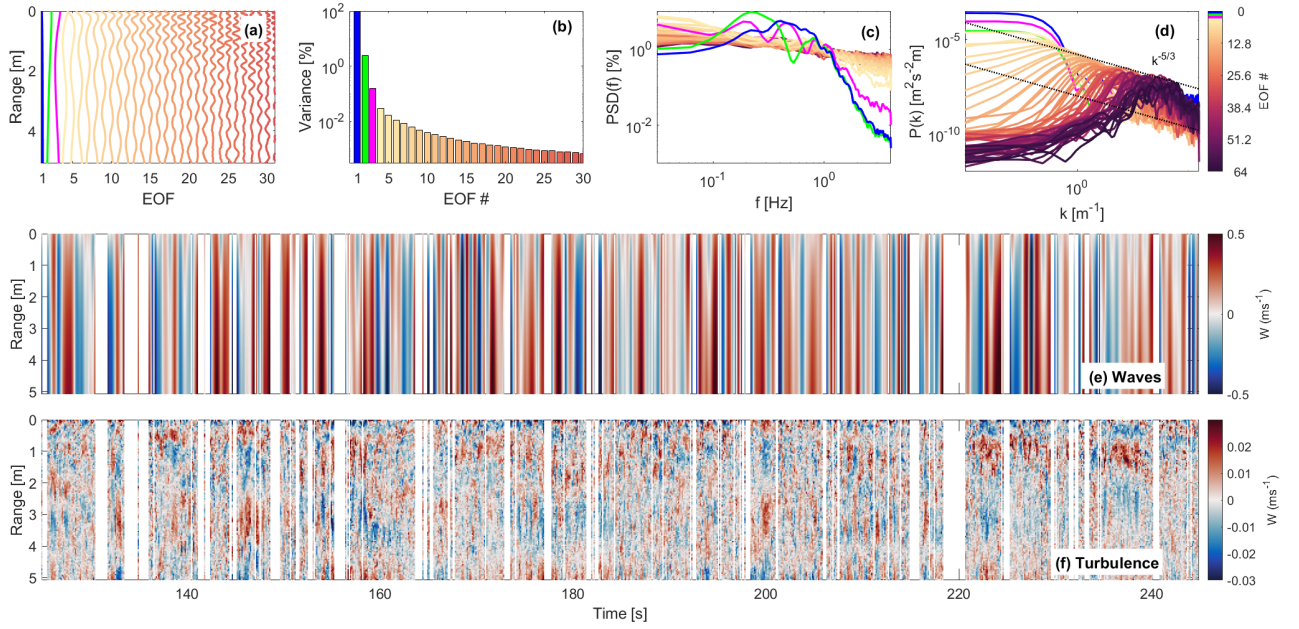
217 velocity profiles as independent spatial measures of the turbulence, rather than as temporal data.
218 We discuss problems with using spectral methods in this application further in section 6.

219 **4. Methodology**

220 In this section we provide a detailed description of the methodology used to compute $\epsilon(z)$ from
221 high resolution (HR) pulse-coherent ADCP velocity data, using the example burst data shown above
222 to illustrate. We begin by computing empirical orthogonal functions (EOFs) of the data, which we
223 use to filter wave orbital motions from the data. We demonstrate that a few of the most energetic
224 EOFs have characteristics of surface gravity waves, while the weaker EOFs have characteristics of
225 inertial subrange turbulence. We proceed to describe the algorithm used to compute the second
226 order velocity structure functions at each depth and compare characteristics of structure functions
227 derived from the unfiltered velocity, EOF filtered velocity and a spatial high-pass filtered velocity.
228 We compute dissipation by least-squares fitting (LSF) the filtered velocity structure functions to
229 Eq. 2 and the unfiltered velocity structure function to Eq. 3, and gauge the validity of each estimate
230 using metrics derived from the coefficients of the fit. Finally, we apply the SF method to the
231 broader SWIFT and Wave Glider datasets to produce over 700 profiles of dissipation under a range
232 of forcing conditions. We show dissipation obtained via the SF method exhibits a clear relationship
233 to near-surface wind speed.

234 *a. Empirical Wave Profiles*

235 Empirical orthogonal function analysis can be a useful tool to describe the statistical modes of
236 variability of a set of observations (Hannachi et al. 2007). EOFs are eigenvectors of the data-data
237 covariance matrix. For ADCP data this constitutes an NxN matrix of the temporal covariance
238 between each possible vertical bin pair, where N is the number of bins. Because the data-data
239 covariance matrix is symmetric, the eigenvectors are orthogonal. Corresponding eigenvalues
240 give the fraction of total variance contained in each EOF, and their time varying amplitudes are
241 obtained by projecting the eigenvectors back onto the original data. The number of EOFs available
242 to describe the data is equal to the number of ADCP depth bins, N. In sum, the data are described
243 as the linear superposition of N statistical orthogonal vertical modes with time varying amplitude.



244 FIG. 3. (a) Empirical orthogonal functions (EOFs) of the quality controlled velocity data from the example
 245 burst sorted by variance, (b) the percent velocity variance described by each EOF, (c) power spectral density of
 246 the time varying amplitude of each EOF, (d) and wavenumber spectra of each EOF. In (a,b) and (c,d) only the
 247 first 30 and 64 EOFs are shown for clarity, respectively. The first three EOFs have characteristics of surface
 248 gravity waves, with low-vertical wavenumbers and spectral peaks in the wave band (blue, green and magenta
 249 bars and lines in (a-f)). Subsequent EOFs have weakly red frequency spectra with no peaks in the wave band,
 250 and are characterized by broadband peaks in wavenumber spectra at progressively higher wavenumbers as their
 251 energy decreases. The slope produced by peaks in the high wavenumber EOFs corresponds to $k^{-5/3}$, consistent
 252 with inertial subrange turbulence. The first three EOFs are used to reconstruct (e) wave profiles which are then
 253 removed from the data to reveal (f) the EOF filtered turbulent velocity.

254 EOFs of along-beam velocity which contain the greatest variance have characteristics expected
 255 of surface gravity waves (Figure 3). Here the EOFs have been sorted by variance, and only the
 256 first 30 EOFs are plotted for clarity. The first EOF contains 98% of the velocity variance, and
 257 describes a velocity profile with no zero crossings and strong shear near the surface (blue lines
 258 in Fig. 3a,b). The power spectrum of its time varying amplitude is dominated by a broadband
 259 peak from 0.1-1 Hz, consistent with motion spectra obtained from the onboard IMU (Fig. 3c).

260 The wavenumber spectrum of the first EOF is red, with a peak at the lowest wavenumber and
261 a significant drop in power for wavenumbers below $\sim 1 \text{ m}^{-1}$ (Fig. 3d). The second and third
262 EOFs are similarly low-mode, with one and two zero crossings respectively, and their frequency
263 spectra are also dominated by energy in the wave band. In contrast, frequency spectra of all lower
264 energy EOFs are comparatively flat with no peaks in the wave band. Their wavenumber spectra are
265 dominated by broadband peaks at progressively higher wavenumbers. The most striking feature of
266 these EOFs is that their energy decreases as $\sim k^{-5/3}$, a hallmark of inertial subrange turbulence.
267 We proceed to reconstruct wave profiles using the first three EOFs, and subtract these from the
268 data to isolate the turbulent component of velocity (Figure 3e,f). Turbulent velocities are $O(0.01$
269 $\text{ms}^{-1})$, with coherent structures of variable size which persist up to 10s of seconds.

275 As emphasized by the EOF wavenumber spectra, removing an empirical wave profile is similar
276 in effect to a spatial high-pass filter. An example velocity profile shows the similarity between
277 the EOF filtered velocity and the 1-m high-passed velocity shown in Figure 4e. The two filtered
278 velocity profiles exhibit the same fluctuations at small scales, but there are $O(1 \text{ m})$ gradients in the
279 EOF turbulence which have been removed by the spatial filter, particularly near the surface. By
280 definition, the spatial filter places an upper limit on the separation scales over which we can fit the
281 structure function to Eq. 2. In all subsequent figures and text, we denote variables derived from
282 the EOF filtered velocity and high-pass filtered velocity with an asterisk and plus sign, respectively
283 (e.g., w^* and w^+ , as in Fig. 4b).

284 b. Ensemble-average Structure Functions

285 To estimate dissipation for each ADCP burst, we compute an ‘ensemble-averaged’ structure
286 function at each desired depth, $D(r)$. We begin by generating M matrices containing velocity
287 differences between all possible data pair combinations, δW_i . Here M is the number of pings in
288 the ensemble (i.e., burst) and $i = 1 \dots M$. If each profile is an Nx1 vector w_i , where N is the number
289 of ADCP range bins, then $\delta W_i = (w_i - w'_i)$ is an NxN matrix. Corresponding separation scale and
290 mean vertical position of each data pair are given by the NxN matrices $R = z - z'$ and $Z = (z + z')/2$,
291 respectively, where z is the Nx1 vector of ADCP bin depths. Next, an NxN structure function
292 matrix is obtained by taking the mean over the ensemble of δW_i^2 , i.e. $D(z, r) = \frac{1}{M} \sum_{i=1}^M \delta W_i^2$. Prior
293 to taking the mean, we attempt to account for any remaining data spikes which have not been

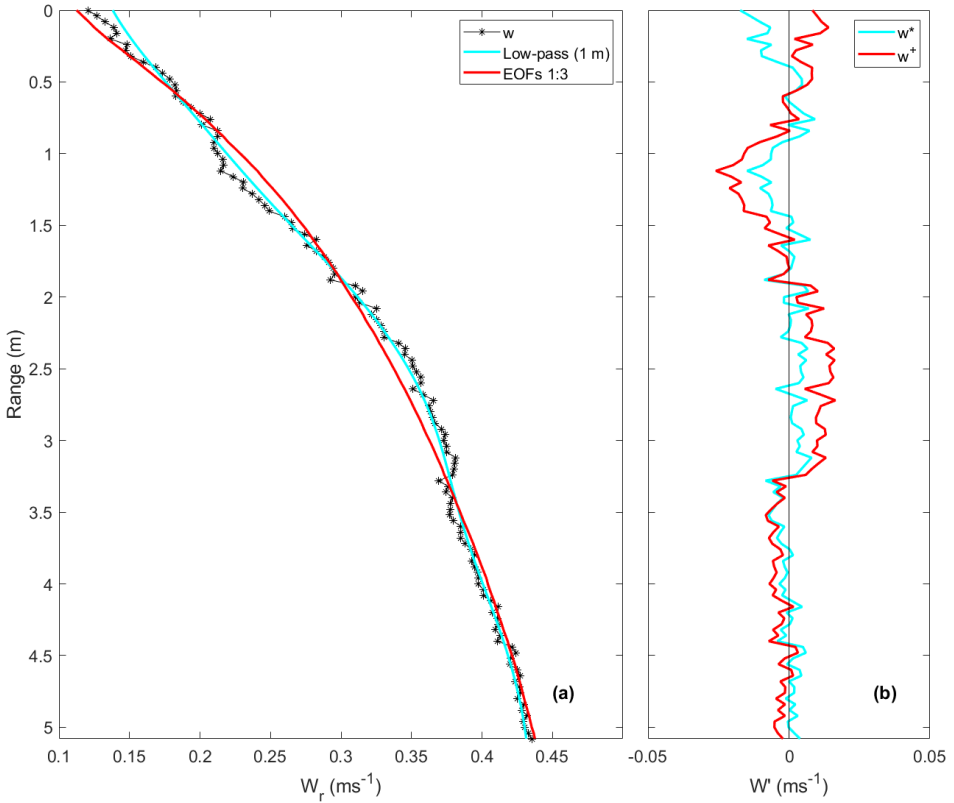
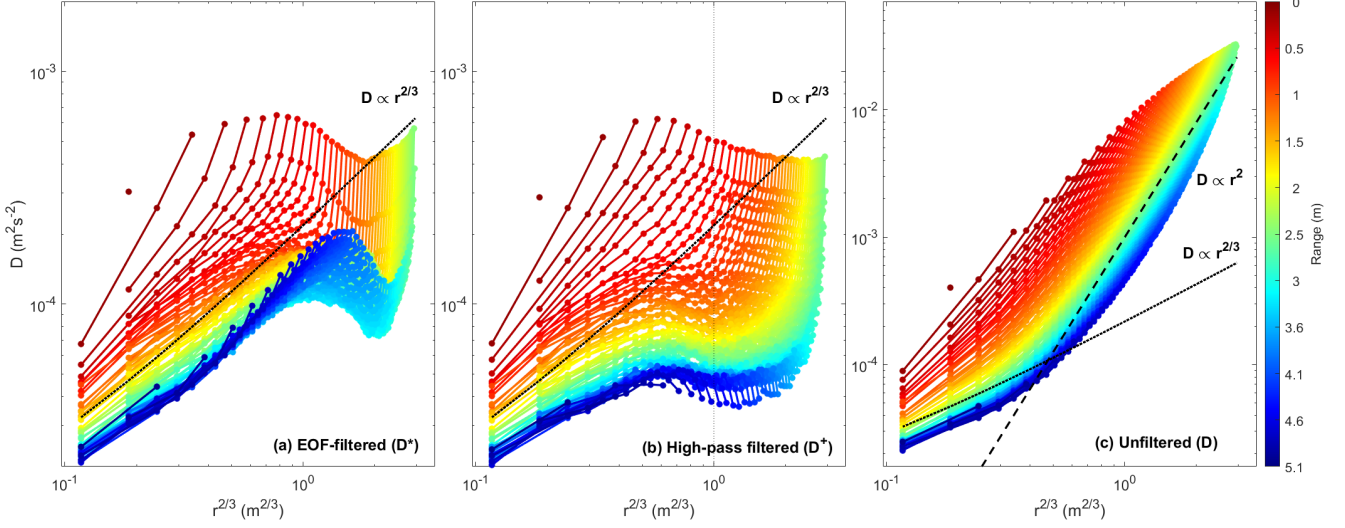


FIG. 4. (a) Example velocity profile produced by a single ADCP ping compared with a 1-m smoothed profile and the empirical wave profile computed from EOFs of the full velocity burst data (black, cyan and red lines, respectively), and (b) the corresponding high-pass and EOF filtered velocity profiles for this ping. Differences between the two methods of filtering are strongest near the surface, where the spatial high pass filter underestimates the near-surface shear of the wave.

filtered by removing δW_i^2 outside 5 standard deviations from the mean of the distribution. Finally, $D(z, r)$ and R are binned to the original ADCP depth bins using Z . The result is a structure function which is dependent on scale alone at each depth, i.e., $D(r)$ (Figure 5).

Consistent with the $k^{-5/3}$ distribution of high-wavenumber EOFs, structure functions of the EOF-filtered turbulent velocity (D^*) increase with separation scale as $\sim r^{2/3}$ up to 1 m, where there is a local maximum (Figure 5a). This maximum may reflect an upper limit to the inertial subrange, but is likely impacted by our choice of which EOFs to include in w^* . The magnitude of D^* decreases with depth, indicating stronger dissipation near the surface. D^* closest to transducer



297 FIG. 5. Second order velocity structure functions $D(r)$ plotted against separation scale (here given as $r^{2/3}$)
 298 as computed from the (a) EOF filtered velocity (D^*), (b) 1-m high-pass filtered velocity (D^+) and (c) unfiltered
 299 velocity (D), colored by depth bin. The two filtered velocity structure functions are very nearly proportional $r^{2/3}$
 300 at small separation scales, while the full velocity structure function is steeper than $r^{2/3}$, approaching r^2 beyond
 301 $r = 1$ m.

307 have slopes slightly steeper than $r^{2/3}$ at the finest scales. At all depths, D^* are much steeper
 308 than $r^{2/3}$ at the maximum possible separation scales, which by definition include the ADCP bins
 309 closest to the transducer. It is possible these bins contain instrument noise which has not been
 310 adequately filtered by our de-spiking routine or that they retain some wave shear. Alternatively,
 311 near-surface turbulence may not conform to the isotropic assumptions of Kolmogorov theory.
 312 Structure functions derived from the high-pass filtered velocity (D^+) are similar to D^* (Fig. 5b).
 313 D^+ exhibit an $r^{2/3}$ dependence at fine scales, decrease in magnitude with depth and increase rapidly
 314 at the greatest separation scales. However, D^+ have a uniform local maxima at $r = 0.5$ m which
 315 has been imposed by the spatial filter.

316 Structure functions computed from the unfiltered velocity (D) exhibit no local maxima and are
317 steeper than $r^{2/3}$ throughout, although they exhibit similar depth dependence to the filtered velocity
318 structure functions (Fig. 5c). At the smallest separation scales, the slope of D is only slightly
319 steeper than $r^{2/3}$ but approaches r^2 with increasing scale (dark red line) as predicted by Scannell
320 et al. (2017). In theory, D is expected to be a linear combination of these two components at all
321 scales, and thus separable by applying Eq. 3 in lieu of Eq. 2. However, the similarity between r^2
322 and $r^{2/3}$ at fine scales emphasized by Fig. 5c foreshadows limitations on the application of Eq. 3
323 when using small integration ranges.

324 The divergence of D^* and D^+ from $r^{2/3}$ at separation scales of ~ 1 m and 0.5 m, respectively,
325 emphasizes the importance of limiting the range of scales included in the least-squares fit. First,
326 including scales which are too large will result in an underestimate of the dissipation due to the
327 decreased slope in D^* and D^+ induced by their local maxima. Second, a major strength of the
328 structure function method is the ability to obtain localized estimates of dissipation. An increase
329 in the separation scale at any depth necessarily reduces the vertical resolution, and risks including
330 data over a range in which ϵ is not uniform. This is especially important closer to the ocean
331 surface, where vertical gradients in dissipation are expected to be strongest. The reason to consider
332 including greater separation scales when fitting Eq. 2 or Eq. 3 to the structure function is to reduce
333 error in the fit (by increasing the number of points). The impact of varying the maximum separation
334 scale is explored further in section 5b.

335 c. Least Squares Estimate of Dissipation

336 As described in section 2, we compute profiles of dissipation from each ADCP burst by fitting the
337 structure function at a given depth by least-squares fitting (LSF) the observed structure function to
338 $D(r) = Ar^{2/3} + N$ (Eq. 2), with an option to include a third term to account for non-turbulent shear
339 of the form Br^2 (Eq. 3). The LSF should be limited to a range of scales assumed to be within the
340 inertial subrange, but the practical considerations described in the previous section suggest stricter
341 limits are likely necessary. A least-squares estimate of dissipation within each depth bin is then
342 given by $\epsilon = (A/C_v^2)^{3/2}$. A consideration when performing the LSF is the effective resolution of
343 the resulting dissipation profile. The resolution is in part dictated by the size of the vertical bins
344 used to determine which $D(z, r)$ are included in the fit at each depth (i.e. which z are included in

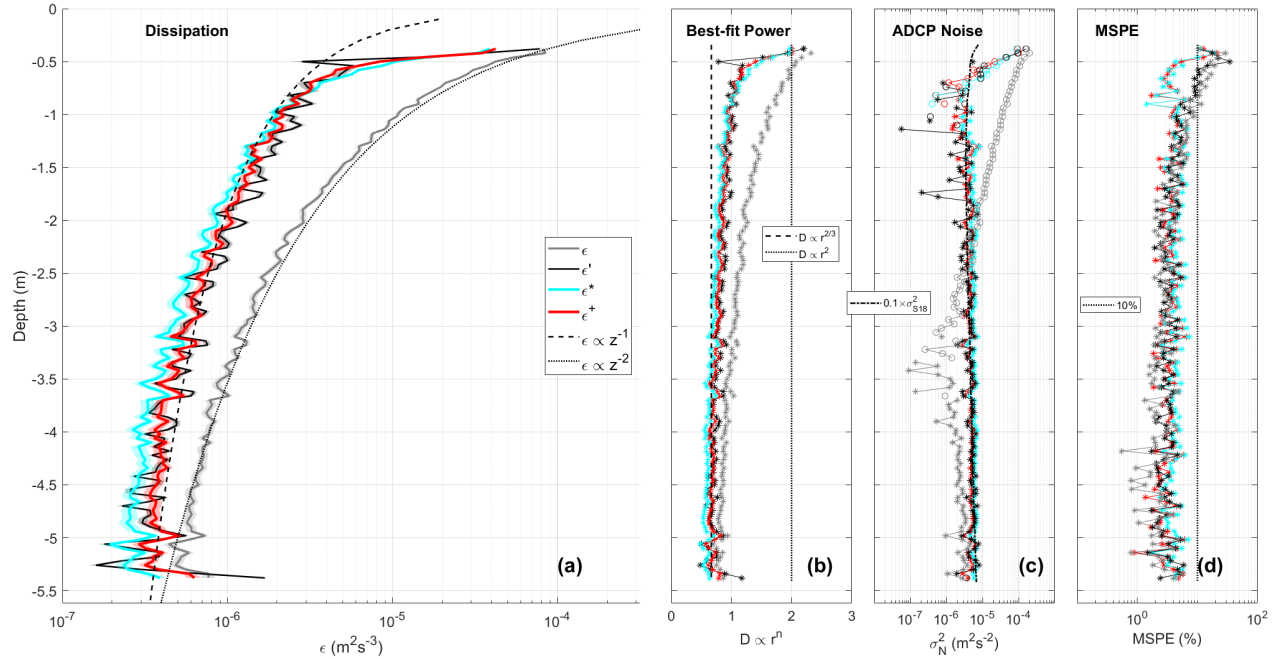
345 the fit). This is not to be confused with the choice of integration range (which r are included in
346 the fit), although both will impact the resolution of the profile. Here we use vertical bins which
347 correspond to the original ADCP bin size in an effort to preserve the vertical resolution of the
348 velocity data.

349 5. Results

350 In this section we present dissipation rate profiles, $\epsilon(z)$, obtained by applying the methodology
351 outlined in section 4 to the velocity data. We begin with detailed results from the example burst.
352 We compute $\epsilon(z)$ by fitting Eq. 2 to the EOF-filtered, high-pass filtered and unfiltered velocities
353 (ϵ^* , ϵ^+ and ϵ respectively). We expect the latter to be biased due to the unfiltered wave velocities
354 in w . We compare these estimates with $\epsilon(z)$ computed by fitting the analytically modified model
355 (Eq. 3) to the unfiltered velocity (denoted with a prime, ϵ'). We provide three quality metrics to
356 gauge the validity of our estimates. The first is the best-fit power-law to $D(r)$, computed as the
357 slope obtained from a linear regression on the logarithms of r and $D(r)$. If the inertial subrange
358 turbulence model for the structure function given by Eq. 2 is valid, we expect $D(r) \propto r^{2/3}$. The
359 second is the estimate of ADCP noise given by the second term in Eq. 2, $N = 2\sigma_N^2$ (Wiles et al.
360 2006). We expect σ_N^2 to be no greater than an a posteriori estimate for the ADCP error derived by
361 Shcherbina et al. (2018), σ_{S18}^2 , which is proportional to the inverse pulse-pair correlation squared.
362 The third quality metric is the mean-square percent error (MSPE) of the LSF to Eq. 2. When $\epsilon(z)$
363 is derived by fitting the modified model (Eq. 3) to the unfiltered velocity structure function, these
364 metrics are computed after removing the estimated shear term from D and refitting the residual to
365 Eq. 2 (residual denoted with a prime, D'). We follow these detailed results with dissipation rate
366 estimates from the broader SWIFT and Wave Glider datasets.

367 In the following we have limited the integration range to $r \leq 0.16$ m, which is the smallest
368 maximum scale which allows for an over-determined problem in the regression in each depth bin.
369 When least-squares fitting D to Eq. 3, we increase the integration range to $r \leq 0.24$ m. We do so
370 to account for the additional degree of freedom in the modified model by maintaining the same
371 proportion of data to unknowns as when using Eq. 2. We explore the impact of varying r_{max} in
372 section 6.

373 a. Dissipation and Regression Coefficients



374 FIG. 6. (a) Profiles of dissipation rate obtained from least-squares fitting the EOF-filtered, high-pass filtered
375 and unfiltered velocity structure functions to Eq. 2 (red, cyan and grey lines), as well as the unfiltered velocity
376 structure function to Eq. 3 (black line). For comparison, the thin dashed and dotted black lines in (a) are curves
377 corresponding to $\epsilon \propto z^{-1}$ and z^{-2} , respectively. Also shown are the corresponding quality metrics; (b) the best-fit
378 power-law to each structure function, (c) the estimate of ADCP noise given by the fit and (d) the mean-square
379 percent error (MSPE) of the fit.

380 Profiles of dissipation rate obtained by fitting Eq. 2 to D^* and D^+ are in close agreement; ϵ^* and
381 ϵ^+ decay in proportion to z^{-1} , decreasing from $\sim 10^{-5} \text{ m}^2\text{s}^{-3}$ at 1 m to $\sim 5 \times 10^{-7} \text{ m}^2\text{s}^{-3}$ at 5 m
382 depth (red and cyan lines in Figure 6a). Above 1 m, ϵ^* and ϵ^+ decay more rapidly than z^{-1} away
383 from the surface, increasingly precipitously by an order of magnitude in the shallowest five bins.
384 In comparison to these estimates, ϵ obtained by fitting Eq. 2 to the unfiltered velocity D is biased
385 high, as expected due to the contribution from wave shear (grey line). The wave-biased estimate
386 also decays more rapidly than the filtered velocity estimates, closely following z^{-2} over the entire
387 profile. Inclusion of the the shear term in the model (i.e. using Eq. 3 instead of Eq. 2) removes

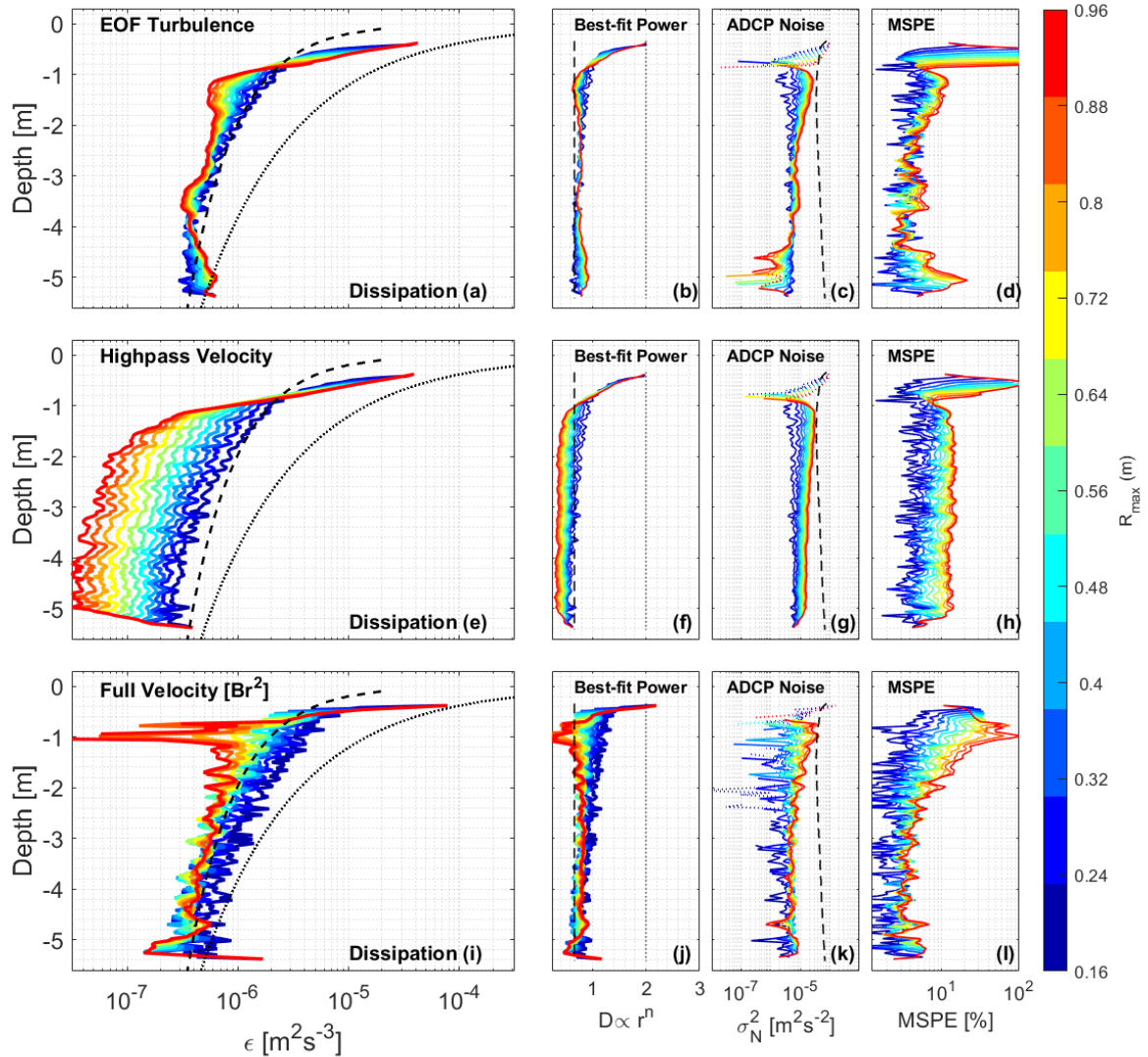
388 this bias and ϵ' is in close agreement with ϵ^+ and ϵ^* , although with discernibly greater along-beam
389 variance (black line).

390 At depths greater than 1 m, the best-fit power-laws to D^* , D^+ and D' are very nearly $r^{2/3}$.
391 Corresponding estimates of ADCP noise from the LSF are an order of magnitude weaker than
392 predicted by σ_{S18}^2 , but increase with depth in proportion to the inverse burst-mean pulse-pair
393 correlation squared as expected (black dashed line in Fig. 6c). The adherence of these metrics to
394 their expected values is quantitatively reflected in the low MSPE of the LSF to D^* , D^+ and D' ,
395 which is less than 10% below 1 m depth. The three quality metrics suggest our estimates of ϵ from
396 all three methods are unbiased below 1 m.

397 Above 1 m, ϵ appears to be biased high. The best-fit power-laws to D^* and D^+ rapidly approach
398 r^2 . These steep slopes generate large, nonphysical negative estimates of the ADCP noise from
399 the LSF (empty circles Fig. 6). Their MSPE increases rapidly above 0.5 m, but only exceeds
400 10% in the shallowest four depth bins. The convergence of ϵ^* and ϵ^+ and their corresponding
401 validity metrics in the upper 1 m to the values given by fitting the wave-biased D to Eq. 2 suggests
402 that retained wave shear may be contributing to bias at depths shallower than 1 m. However, this
403 inference is at odds with the results of fitting the wave-biased D to Eq. 3 (modified model), which
404 we expect to account for wave shear. Instead, the best-fit power-law to D' (shear term from the LSF
405 removed from D) still increases rapidly from $r^{2/3}$ to r^2 , the corresponding ADCP noise estimate
406 is negative, and the MSPE exceeds 10%. These characteristics suggest that the near-surface bias
407 in ϵ is either due to poor ADCP quality close to the transducer, or that turbulence observed in this
408 depth range does not support the statistical assumptions of Kolmogorov theory.

409 b. Sensitivity to Integration Scales

415 To reduce uncertainty in our estimates of $\epsilon(z)$ we may include more data in each LSF by
416 increasing the maximum separation scale (r_{max}) over which the fit is applied in each depth bin,
417 at the expense of vertical resolution. Potential issues include exceeding the upper limit of the
418 inertial subrange and spreading the influence of any low quality ADCP bins. Figure 7 illustrates
419 how the three different estimates of ϵ are impacted by increasing r_{max} up to 0.64 m (16 vertical
420 bins). ϵ^* decreases by a factor of 2 (except in the upper and lower 1 m of the profile) and develops
421 O(1 m) vertical structure. This is consistent with the corresponding best-fit power to D^* , which



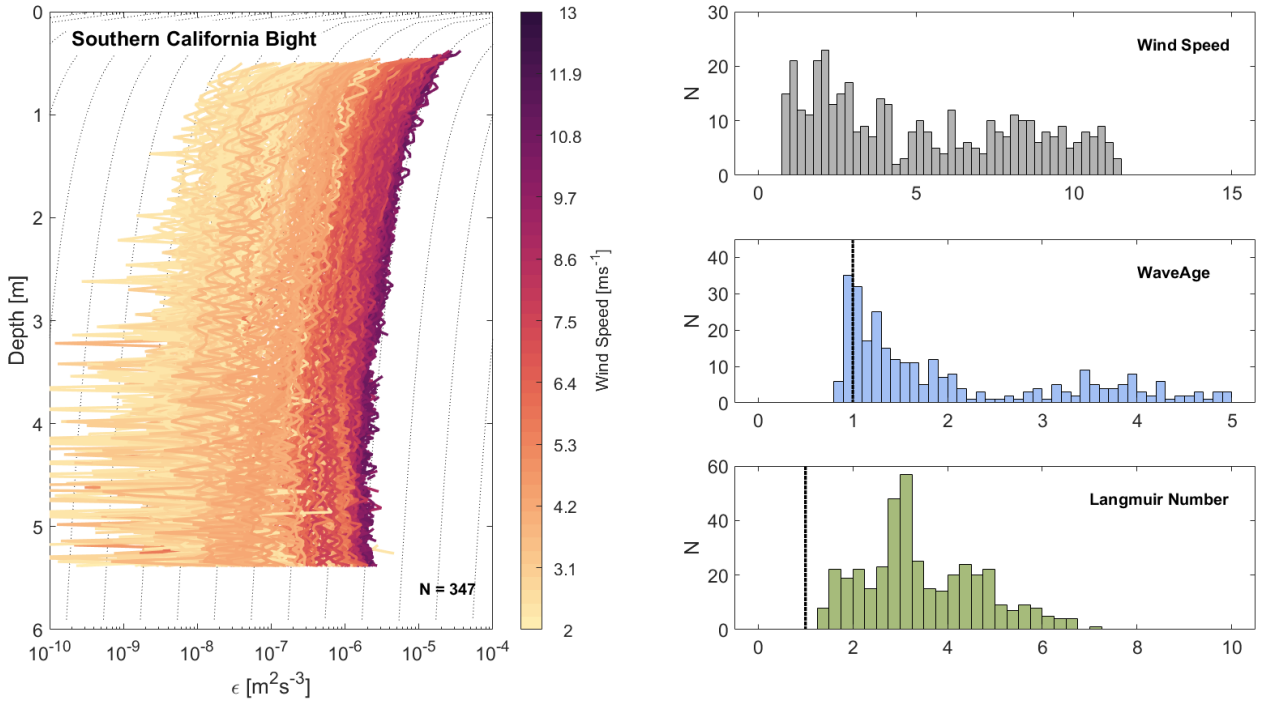
410 FIG. 7. Impact of varying the maximum separation scale included in the LSF on (a, e, i) dissipation rate, (b,
 411 f, j) best-fit power to the structure function, (c, g, k) the estimate of ADCP noise produced by the fit and (d,
 412 h, l) the MSPE of the fit. Top row (a-d), middle row (e-h) and bottom row (j-l) show results derived from the
 413 EOF filtered velocity, high-pass filtered velocity and unfiltered velocity, respectively. Line colors correspond to
 414 maximum separation scale. In all cases, the MSPE increases with integration range.

remains very close to $r^{2/3}$. In contrast, ϵ^+ decreases by an order of magnitude uniformly with depth. Corresponding estimates of ADCP noise and MSPE increase with r_{max} as the shape of the structure function becomes progressively shallower than $r^{2/3}$. These differences between ϵ^* and ϵ^+ reflect the different local maxima in D^* and D^+ (Fig. 5). The latter occur at a precise separation scale of 0.5 m and so ϵ^+ decreases uniformly with increasing r_{max} . The vertical structure which appears in ϵ^* is due to the variability in the local maxima of D^* . Interestingly, ϵ' decreases uniformly with increasing r_{max} but appears to converge to the value given by the initial estimates of ϵ^+ and ϵ^* (i.e. using $r_{max} = 0.16$ m). This is consistent with the best-fit power to D' which converges to $r^{2/3}$. In all cases, the depth ranges influenced by the biased near surface bins increases with r_{max} . These results of varying r_{max} confirm that it is prudent to keep the integration scale as small as reasonable, except possibly when fitting the analytically modified model (Eq. 3) to the data.

433 c. Application to SWIFT and WaveGlider Datasets

Application of the structure function methodology to the broader SWIFT and Wave Glider datasets reveals a clear relationship between dissipation rate and near surface wind speed (Figures 8 and 9). Shown in each are $\epsilon^*(z)$ derived from the EOF filtered velocity, colored by 1-m wind speed. As in the example burst, the most energetic three EOFs of each burst have been used to produce a wave profile which is removed from the data. Here we have quality controlled the dissipation estimates by applying a maximum allowed MSPE of 10%. The primary consequence of this threshold is to remove bins in the very near surface. In total there are 347 profiles from the SWIFTs and 388 profiles from the Wave Glider.

In both datasets, dissipation increases in magnitude with increasing wind speed and profiles follow $\sim z^{-1}$, except very close to the surface ($z < 1$ m) where the profiles are steeper. This is clearest at wind speeds greater than $\sim 5 \text{ ms}^{-1}$. Wind speeds ranged from $1\text{-}12 \text{ ms}^{-1}$ in the Southern California Bight, and corresponding ϵ^* ranged from $\sim 10^{-9} - 10^{-5} \text{ m}^2\text{s}^{-3}$ in the upper few meters. Dissipation estimates corresponding to especially weak winds (less than 5 ms^{-1}) are substantially noisier than those corresponding to strong winds, but still exhibit sorting based on wind speed. Wind speeds in the Southern Ocean ranged from $5\text{-}15 \text{ ms}^{-1}$, thus there are no low-wind estimates of dissipation rate in the Wave Glider dataset. In general, ϵ^* estimates from the Southern Ocean are weaker than those obtained in the Southern California Bight at the same wind speeds. Histograms



434 FIG. 8. Profiles of dissipation rate obtained by applying the SF method to EOF filtered velocity data obtained
 435 from SWIFT drifters in the Southern California Bight in March and April of 2017. Profiles of ϵ are colored by
 436 1-m wind speed. The forcing conditions during the observation period are summarized by histograms of wind
 437 speed (grey), wave age (blue) and Langmuir number (green).

460 of wave age suggest that these differences may be due to the comparatively young seas in the
 461 Southern California Bight. Turbulent Langmuir numbers during both sets of observations were
 462 greater than 1, but they were lower on average in the Southern California Bight and so conditions
 463 may have been more favorable to Langmuir overturning as well.

464 Dissipation profiles derived from the high-pass filtered velocity (ϵ^+) are very similar to ϵ^* , except
 465 in the upper 1 m (Figure 10b). We use data from the Southern California Bight to compare the
 466 different methods of estimating ϵ due to the greater range of wind speeds observed there. Profiles of
 467 ϵ^+ are steeper than ϵ^* near the surface, deviating from z^{-1} at increasing depth with decreasing wind
 468 speed. In contrast to ϵ^* and ϵ^+ , dissipation derived from the unfiltered velocity using the modified
 469 structure function model (ϵ') appear to follow z^{-1} at high wind speeds, but these estimates are
 470 considerably noisier and not as neatly sorted by wind speed (Fig.10b). There is almost no discernible

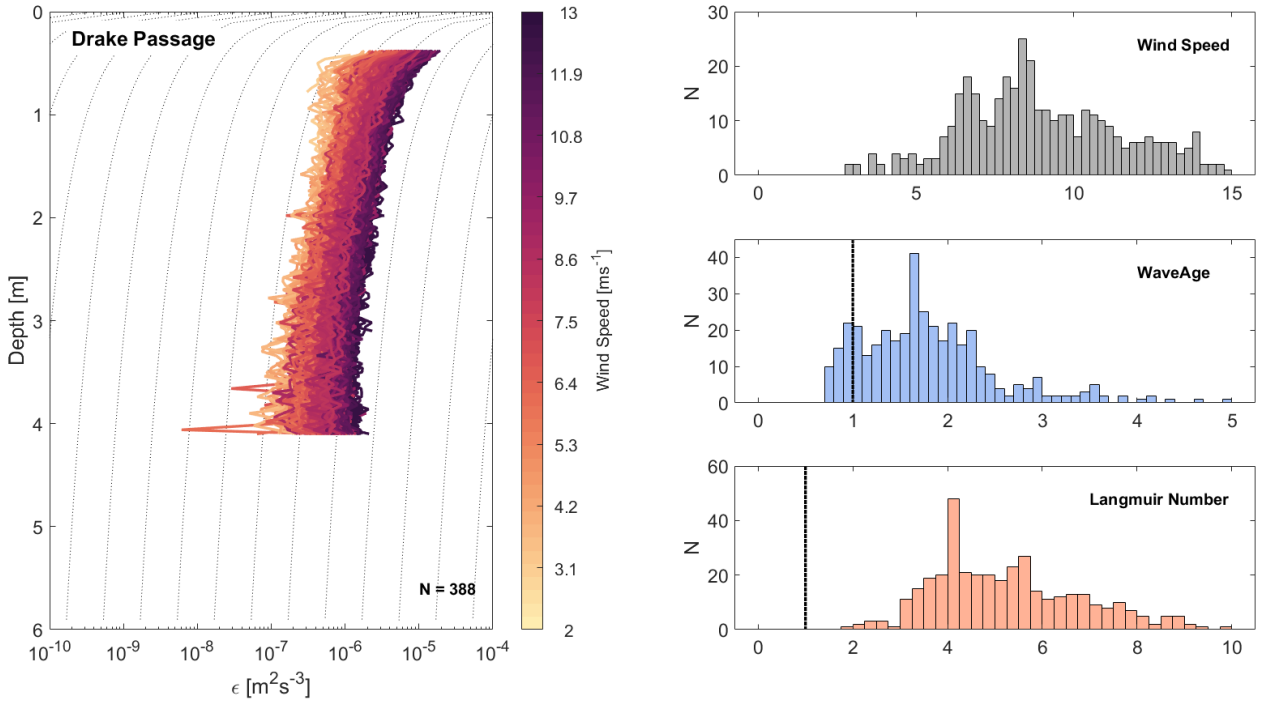
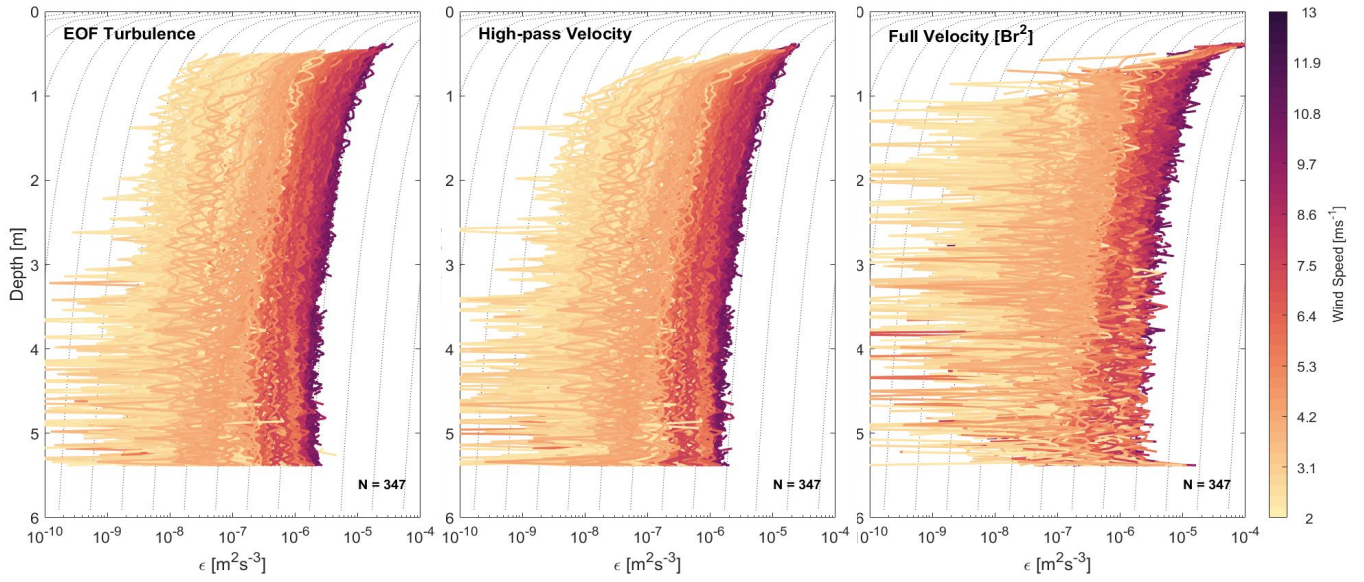


FIG. 9. As in Figure 8, but for the Wave Glider data collected in the Southern Ocean.

wind speed dependence at the base of the profile. Mean MSPE of the analytically modified LSF to the unfiltered velocity is 12%, compared to 5% for both the EOF-filtered velocity and 1-m high-pass filtered velocity derived estimates.

6. Discussion

In this section we discuss our results before making final recommendations for analysis. We compare dissipation estimates which result from pre-filtering the velocity data to remove wave shear with those from the analytically modified SF method. Our analysis suggests the former method produces estimates of $\epsilon(z)$ with reduced noise and a clear relationship to local wind speeds even under weak forcing conditions. We then test the sensitivity of ϵ^* to varying the number of EOFs used to construct an empirical wave profile and discuss limitations of the EOF filtering technique. Finally we discuss why spectral methods of estimating dissipation are not likely to be suitable for data obtained with a surface following platform, further emphasizing the advantages of the structure function method in this particular application. We follow these discussions with a summary of our methodology and recommendations for analysis.



438 FIG. 10. Comparison between the different methods of estimating ϵ over the entire SWIFT dataset obtained
 439 in the Southern California Bight using the (left) EOF filtered velocity, (middle) high-pass filtered velocity and
 440 (right) unfiltered velocity. The two pre-filtered estimates are largely the same, with clear wind sorting. The
 441 unfiltered estimate is substantially noisier, which obscures much of the wind sorting at depth and at low wind
 442 speeds.

485 *a. Advantages of pre-filtering to remove wave bias*

486 An important result of our analysis is the reduced noise and clear wind sorting of dissipation
 487 profiles derived from velocity data which has been pre-filtered to remove wave bias, compared to
 488 those derived from the modified LSF fit formulated by Scannell et al. (2017) (Fig. 10). The superior
 489 performance of the filtering method is in part due to the limit on integration range imposed by
 490 strong along-beam variability in epsilon over the upper few meters of the ocean. The mean square
 491 percent error of fitting r^2 against $r^{2/3}$ is less than 50% for $r_{max} \leq 0.1$, but increases exponentially
 492 with increasing integration range (not shown). Distinguishing between r^2 and $r^{2/3}$ is substantially
 493 more difficult at finer scales and will be more sensitive to noise in the structure function. The

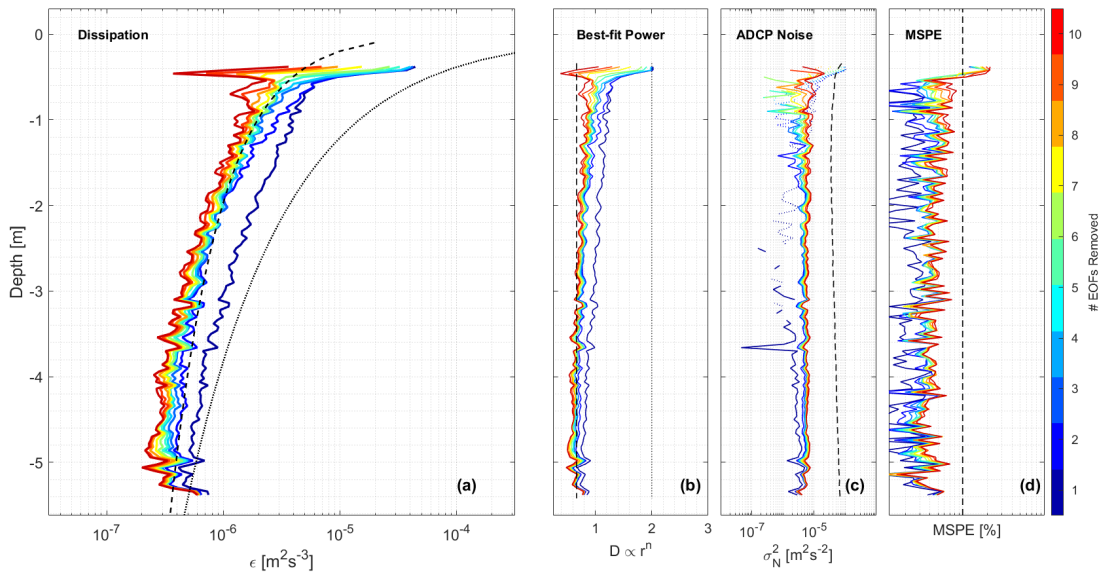
494 modified structure function model is also inherently more sensitive to noise due to the additional
495 degree of freedom introduced by the r^2 term (DOF = 4). The number of points used in the fit is
496 less than 10 for $r \leq 0.2$ m.

497 More generally, the fundamental advantage of the pre-filtering techniques is that they are em-
498 pirical and thus largely agnostic to the structure of the background flow. For example, the only
499 assumption in performing the spatial high-pass is that there is a separation in wavenumber space
500 between non-turbulent shear and inertial subrange turbulence, which is consistent with the under-
501 lying Kolmogorov theory. This assumption is likely to fail very close to the surface, as in our
502 example, where non-turbulent shear is strongest and edge effects of the filter are felt (Fig. 2e).
503 In a related fashion, the EOF filter technique rests on the assumption that the dominant modes of
504 variability are non-turbulent. In the case of surface waves with large vertical wavenumbers this has
505 a similar effect as a spatial high-pass, but the separation in wavenumber space is not a requirement
506 for the EOF filter to be effective. We discuss advantages and limitations of the EOF analysis further
507 in the next section.

508 The analytic formulation of the modified SF method is a strength specifically in the case of
509 non-turbulent shear which is a straightforward superposition of linear surface gravity waves. The
510 approximation given by Scannell et al. (2017) that leads to a structure function of the form r^2 is
511 valid within 2% for the range of waves observed in these two datasets. However, if the background
512 shear does not conform to the r^2 approximation the modified model will fail to account for bias
513 in the structure function. This is more likely to occur in the very near surface, due to complex
514 surface phenomena such as wave-current interactions, convective overturns, Langmuir turbulence,
515 and diurnal stratified shear layers. In summary, the modified SF method is likely to perform
516 well at depth in an environment dominated by approximately linear background shear, and which
517 enables large integration ranges. In contrast, the large range of ϵ which imposes a limitation on the
518 integration ranges and complex physical phenomena characterising the near surface region require
519 empirical filtering techniques which remove non-turbulent shear prior to computing the structure
520 function.

521 *b. Sensitivity and Limitations of EOF analysis*

522 Surface gravity waves observed by down-looking ADCPs are well suited for EOF analysis because
 523 they are in-phase across the ‘array’ of ADCP depth bins as they propagate past the instrument.
 524 Further, the high resolution of the data means there are a large number of modes available to
 525 describe the system. The motion of the platform leads to horizontal beam displacements up to 1 m
 526 between pings, but surface gravity waves with peak frequencies $O(0.1 \text{ Hz})$ have wavelengths $O(10$
 527 $\text{m})$ and subsequent space-time aliasing is small. Removing a few dominant modes from the data is
 528 akin to removing a strong background “mean” from each profile, with some near surface curvature
 529 that is difficult to model analytically (Fig. 4). This is why EOFs are so similar to the spatial high
 530 pass. The “residual” is obviously not noise despite the bulk of the variance being contained in the
 531 first few EOFs (Fig. 3).



532 FIG. 11. Impact of varying the number of low-mode EOFs used to construct the wave profile which is then
 533 removed from the data in the EOF filtering method. Subplots are as in Figure 7, but here colored by number of
 534 EOFs removed from the data. The estimate of ϵ is robust to increasing the number of EOFs removed up to ~ 6
 535 for this example burst.

536 The main weakness in the EOF filtering technique is the subjective choice of what number of
 537 low-mode EOFs to remove from the data. In our example burst, frequency spectra of the EOF

amplitudes reveal that only the first three EOFs have peaks in the wave band, thus providing a natural cutoff (Fig. 3). Such a detailed examination of the EOFs of each ADCP burst is not practical for bulk processing. However varying the number of low-mode EOFs removed in the filter in the example burst case suggests that dissipation is likely robust to the choice between ~ 2 to 6 EOFs (Figure 11). The shape and magnitude of the profile is generally preserved up to the removal of 10 low-mode EOFs, except for a large decrease in ϵ around 0.5 m when more than 6 EOFs are removed (Fig. 11a). In fact, the estimate of $\epsilon(z)$ appears to improve when a few additional EOFs are removed, particularly near the surface where $\epsilon(z)$ was initially biased (Fig. 6). The best-fit power to the filtered velocity structure function converges to $r^{2/3}$ and the estimate of ADCP noise becomes positive. However, MSPE increases slightly as additional low-mode EOFs are removed, likely due to the spatial-filter effect which is a consequence of the EOF sorting in wavenumber space (i.e. the redness of the wavenumber spectra). The removal of each additional low-mode EOF moves the local maximum in D^* to a smaller scale. The robustness of the dissipation estimate is not surprising, given the small integration range used in the LSF. A fundamental assumption of the SF method of estimating dissipation is that the contribution to the structure function at each scale is primarily due to turbulent eddies at that scale, so even unintentional filtering of the largest scale turbulent velocities should not egregiously alter the results.

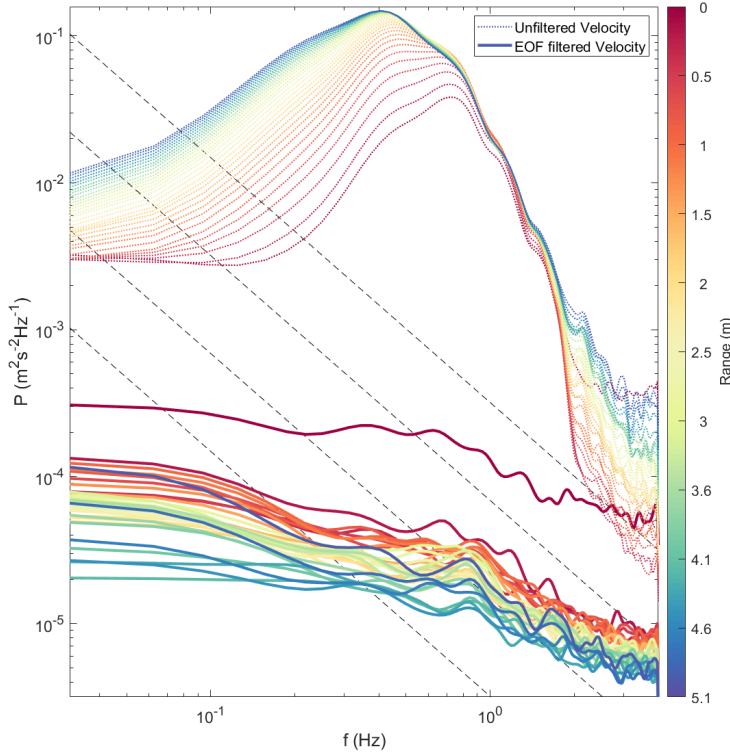
Finally, there are conditions under which we might expect the EOF filtering technique to fail. A weakness of the traditional EOF analysis is that signals must be in phase across the array due to the reliance on covariance at zero time lag, and so individual EOFs cannot represent the variability of vertically propagating modes (Merrifield and Guza 1990). Strong signals which propagate rapidly over the course of a burst may not be well described by low-mode EOFs, or may require the removal of a much greater number of low-mode EOFs. A few examples include internal waves, bubble plumes and rapidly deepening shear layers. Potential improvements to the EOF filtering technique may include exploring alternatives which attempt to mitigate these phase-locked limitations, such as complex EOFs (Merrifield and Guza 1990).

564 c. Instrument motion impact on spectral methods

565 Strong platform motion induced by surface waves, combined with data contamination by wave
566 orbital velocities, make it difficult to apply spectral techniques of estimating dissipation in the

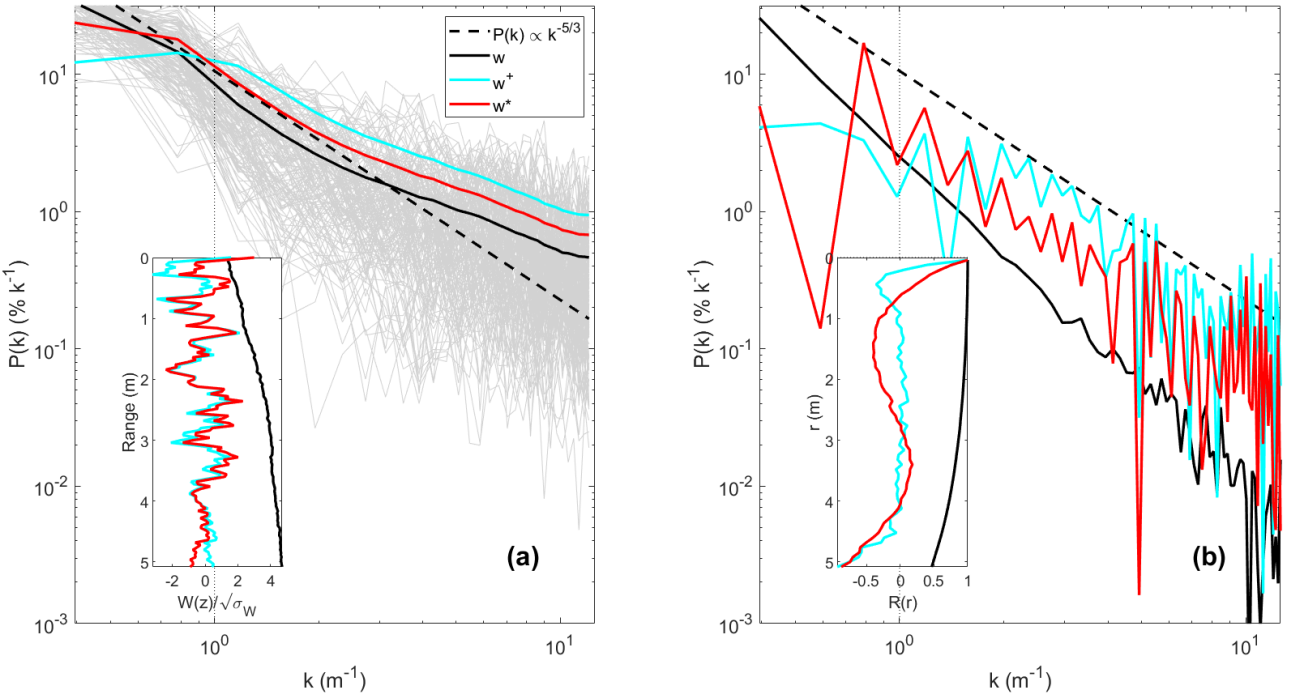
near-surface. Here we discuss reasons the spectral methods are likely to produce estimates of $\epsilon(z)$ with high error, using the example burst data to illustrate. The two main challenges are 1) properly defining an advective velocity for a Lagrangian platform and 2) incoherence of the observed turbulent velocity fluctuations in time. The former makes the frozen-field assumption weak, and the latter smears the energy in frequency space. Previous authors have dealt with the problem of defining an advective velocity for a surface following platform by obtaining an estimate of large-scale eddy self-advection from the velocity data itself (e.g. Zippel et al. 2018), though this method does not account for advection by wave orbital motions. However, even when wave orbital velocities are successfully removed from the data, the latter problem is likely intractable. Figure 12 shows frequency spectra computed from each ADCP bin in the example burst before and after wave orbital velocities are removed from each profile using the EOF filtering technique. Waves contribute spurious energy at all frequencies, which leads to an increase in energy with increasing distance from the transducer even at the high-frequency end of the spectra (i.e. away from the surface, pale lines). An increase in dissipation rate away from the surface is almost certainly not physical. Removing wave orbital velocities from the data reverses the direction of increasing energy (now towards the surface, bold lines) and removes the broadband wave peak centered at 0.4 Hz. However, high-frequency tails of the residual spectra are much shallower than $f^{-5/3}$, consistent with smearing in frequency space due to the motion of the instrument. Tilt angles vary on average by a few to tens of degrees each ping, corresponding to horizontal displacement of the ADCP beam by tens of centimeters up to 1 m. Near-surface length scales of turbulence are naturally limited by proximity to the sea-surface to a few meters, thus horizontal displacement O(0.1 m) between pings likely smears a large portion of the inertial subrange.

Along-beam wavenumber spectra would not be sensitive to the motion-induced coherence issues inherent in frequency spectra. However, this method produces a single timeseries of dissipation rate for the entire profile and is thus better suited for environments where the dissipation rate is expected to be constant over the profile range. Shcherbina et al. (2018) demonstrated the effectiveness of the wavenumber spectra method at depth using Signature 1000 HR ADCP data obtained from a sub-surface Lagrangian float. Corresponding burst-average wavenumber spectra demonstrate a clear $k^{-5/3}$ dependence. The authors also show how ϵ profiles may be obtained during periods when the float is actively profiling by applying the frozen-field assumption to velocity frequency



589 FIG. 12. Velocity frequency spectra computed from the example burst as a function of depth bin, before and
 590 after wave orbital velocities are removed using the EOF filter technique (faded and bold lines, respectively).
 591 Initially, the spectra are contaminated by wave velocities across the entire resolved frequency range. After the
 592 wave velocities are removed, the residual spectra are much flatter than the expected $f^{-5/3}$ slope (dashed lines)
 593 expected for inertial subrange turbulence.

609 spectra (see their Figure 8). This approach is not feasible in our application due to the strong
 610 motion of the platform with respect to the water, as demonstrated above. It is also likely our 1D
 611 (along-beam only) de-spiking routine under-performs the method used by Shcherbina et al. (2018),
 612 and the data retain some number of spikes. In their method, the ping-to-ping coherence of the
 613 observed turbulent velocities is leveraged to identify and fill data spikes (appropriately designated
 614 ‘2D phase unwrapping’). In our data, wavenumber spectra computed from individual velocity
 615 profiles fluctuate wildly between an apparent noise floor and $k^{-5/3}$ at high wavenumbers (Figure
 616 13a, thin grey lines). The resultant burst-averaged wavenumber spectra are shallower than $k^{-5/3}$
 617 (bold lines).



594 FIG. 13. Burst averaged along-beam velocity wavenumber spectra, computed (a) directly via Fourier transform
 595 of the along-beam velocity (thin grey lines) and then burst-averaged (bold lines), and computed (b) from
 596 the Fourier transform of the burst-averaged data-data pair autocorrelation function (bold lines). Inset in (a)
 597 shows examples of the velocity profiles on which the Fourier transform is performed. Inset in (b) shows the
 598 burst-averaged autocorrelation function on which the Fourier transform is performed. Black, red and cyan lines
 599 correspond to the unfiltered (but quality controlled) velocity, EOF-filtered velocity and high-pass filtered velocity,
 600 respectively.

618 An alternative method of computing wavenumber spectra is to take the Fourier transform of the
 619 along-beam autocorrelation. This method allows for averaging in time prior to performing the
 620 transform and is therefore more analogous to the structure function method, although it would
 621 still produce a constant ϵ instead of a profile. The large N reduces the impact of any retained
 622 spikes and the resultant wavenumber spectrum has a clear $k^{-5/3}$ dependence at high wavenumbers
 623 (Fig. 13b). The autocorrelation derived wavenumber spectra emphasizes a major strength of the
 624 structure function calculation; robustness in the face of poor data quality. Spectral methods require
 625 continuous timeseries and spikes must be filled in some fashion, thus data with a high percentage

626 of spikes are unusable. Because velocity differences are first averaged in time, structure functions
627 can be computed even with a low percentage of “good” data. The quality metrics described in
628 section 4 are then available to asses the accuracy of subsequent dissipation estimates.

629 **7. Summary and Recommendations for Analysis**

630 The primary contribution of this study is an update to the methodology of Thomson (2012) to
631 compute turbulent dissipation rate from pulse-coherent high-resolution (HR) ADCP data collected
632 using surface following platforms, building on the work of Scannell et al. (2017) to account for the
633 bias in $\epsilon(z)$ generated by wave shear in the very near surface. As an alternative to the modified
634 SF method put forward by those authors, we isolate the turbulent velocity signal from the wave
635 orbital velocity using empirical methods. We compare two filtering techniques; a simple spatial
636 filter which removes energy concentrated at low wavenumbers, and a modal filter which removes
637 a time dependent wave profile computed using empirical orthogonal functions (EOFs) of the data.
638 Our results indicate that the empirical filtering methods produce superior dissipation estimates
639 with a clear relationship to local wind forcing which appears to be obscured by greater noise in the
640 dissipation estimates obtained using the modified SF method. We attribute this discrepancy to the
641 small integration scales necessitated by proximity to the sea-surface, which constrains the number
642 of points in the LSF. The analytic modification introduces an additional term to the structure
643 function model and is therefore more sensitive to outliers due to the additional degree of freedom,
644 while large integration ranges are required to distinguish between the wave and turbulent terms.
645 Based on the results of this study, we recommend the following steps to compute dissipation from
646 bursts of high-resolution (HR) velocity data obtained using pulse-coherent mode on the central
647 beam of a surface-following platform mounted ADCP:

- 648 1. De-spike data using an along-beam median filter and a maximum velocity anomaly equal to
649 half the phase wrapping velocity (dependent on the instrument configuration, see Shcherbina
650 et al. (2018) section 2c).
- 651 • Best practice is to replace data spikes with NaN, since the structure function will be
652 robust to missing data. However, interpolation may be necessary to retain enough points
653 for a robust estimate of the EOFs (see step 2).

654 2. Filter out non-turbulent shear by removing at least the two most energetic EOFs of the data.

- 655 • Best practice is to examine the EOFs to determine an appropriate cutoff, though this may
656 be impractical for bulk processing.
- 657 • Interpolation through data spikes may be helpful in estimating the low-mode EOFs, but
658 these points should be removed prior to computing the structure function.
- 659 • Alternatively, perform a spatial high-pass to remove low-mode shear. This method will
660 likely retain more surface wave shear with small decay scales in the very near surface
661 than the EOF filter technique.

662 3. Compute squared velocity difference matrices for each along-beam velocity profile and average
663 in time to produce a single burst-averaged second order structure function matrix with bin-pair
664 mean depth and separation scale dependence.

- 665 • Best practice is to remove points which contain interpolated data prior to averaging.
666 Interpolation is likely to alter the scale dependence of the subsequent structure function
667 (i.e. by removing energy at bin-scale separation)

668 4. Bin the structure function by depth and perform a least-squares fit against $r^{2/3}$ within each bin
669 over a limited range of separation scales to obtain $\epsilon(z)$ from Eq. 2.

- 670 • Best practice is to limit the maximum separation scale included in the fit as much as
671 possible while still allowing for an over-determined problem when along-beam variation
672 in ϵ is expected to be large. Some iteration may be required to determine the ideal
673 integration range.

674 5. Quality control $\epsilon(z)$ using the mean-square percent error of the LSF.

675 Throughout the manuscript we have commented on various user choices which may impact the
676 results. The most significant is integration range, but others include depth-bin size and number of
677 EOFs included in the filter (alternatively the scale of the spatial high pass filter). An additional
678 sensitivity not explored in this manuscript are various definitions of the ensemble average, including
679 the median and mean-of-the-log of the squared velocity differences. An argument may be made
680 that the latter approach is more appropriate in light of the logarithmic distribution of dissipation

scales, particularly in the near surface environment (Gargett 1999). We have presented quality metrics to help evaluate the validity of $\epsilon(z)$, but a lingering uncertainty is what thresholds may be appropriate to apply. For example, in our data a threshold MSPE of 10% appeared organically but there is no inherent physical reason this value may distinguish between good and poor quality estimates. Although the relationship with local wind forcing provides confidence in our estimates, further improvements in this methodology would be significantly enhanced by comparison with direct in-situ measurements of $\epsilon(z)$, wave-breaking crest distributions $\Lambda(c)$, or other hydrographic information such as stratification and horizontal velocity shear which can further help constrain the values we should expect from our analysis.

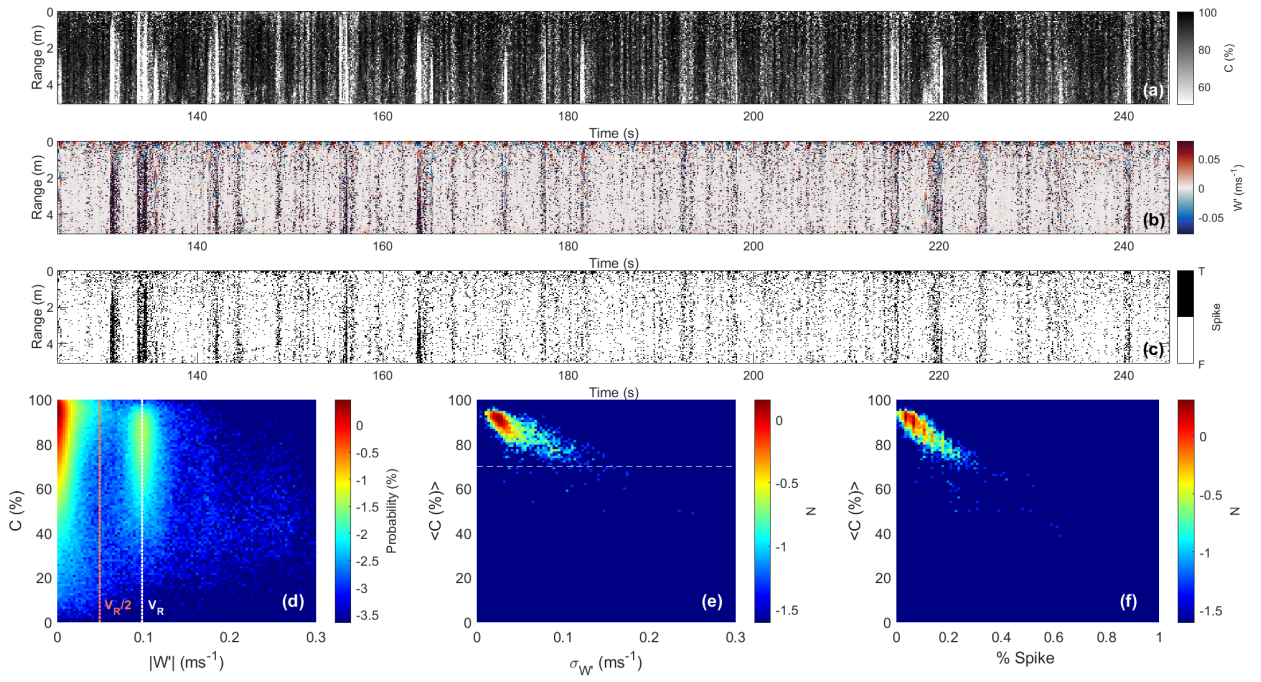
690 *Acknowledgments.* We would like to thank APL field engineers Joe Talbert and Alex de Klerk
691 for their work to prepare, test and deploy the SWIFTs and Wave Glider, as well as the captains
692 and crews of the R/V L. M. Gould and R/V R. G. Sproul for deployment and recovery of both
693 instruments. We would also like to thank Eric D’Asaro and Andrey Shcherbina for insightful
694 comments which improved the manuscript, as well as suggestions for future improvements to the
695 methodology. Funding for the Wave Glider work in the Southern Ocean was provided by the
696 National Science Foundation (OPP-1853291), while the SWIFT work in the Southern California
697 Bight was conducted under NAVSEA contract N0002419F8705.

698 *Data availability statement.* The SWIFT data used in this study can be downloaded at
699 the following (temporary, to be updated with permanent link prior to publishing) link:
700 <https://datadryad.org/stash/share/BbWkkUvZFMMpNhBxw7T8qtYXsaBTzxNYgjv4mJ3dmAA>.
701 The Wave Glider data can be found at <http://hdl.handle.net/1773/49469>. The codes used in data
702 processing are publicly available at <https://github.com/jthomson-apluw/SWIFT-codes>.

703 **APPENDIX**

704 **Raw Data Quality Control**

711 Strong velocity spikes generate an inextricable bias in the burst-average structure function due to
712 the squaring of velocity differences. Thus de-spiking the velocity prior to analysis is necessary to
713 reduce bias in the dissipation estimate. In pulse-coherent mode, along-beam velocity measured by
714 the ADCP is a function of the phase shift between the pulse-pair echo with respect to their initial lag
715 time. A well known limitation of this method is ambiguity in the velocity introduced by phase shifts
716 exceeding 2π , i.e. velocities which exceed a corresponding V_R . For the ADCP configuration used in
717 this study, V_R is $\sim 0.1 \text{ ms}^{-1}$. High velocities are susceptible to “phase-wrapping”, which manifests
718 as velocity spikes equal to \pm an integer number of V_R . Ambiguity in the phase shift can also arise
719 when the magnitude of the peak in lagged pulse-pair correlation (used to identify the phase shift)
720 is weak. Figure A1 shows the data spikes identified in the example burst explored in sections 3 and
721 4, and their relationship to pulse-pair correlation. Correlation generally about 80%, but low value
722 points are littered throughout and the correlation over an entire ping will occasionally drop abruptly
723 below 50% (Fig. A1a). These drop outs can last for $\sim 1\text{-}10$ pings (up to 1 second), during which
724 the velocity is overwhelmed by strong spiking throughout the profile. Spikes are identified my first



705 FIG. A1. Example of the despiking routine applied to the pulse-coherent Nortek Signature 1000 ADCP data.
 706 Shown are (a) pulse-pair correlation, (b) residual velocity after a 1-m median filter has been removed, (c) data
 707 spikes, identified as residual velocities greater than $\pm V_R/2$. Also shown are probability density functions of the
 708 data as a function of (d) residual velocity magnitude and pulse-pair correlation, (e) along-beam residual velocity
 709 variance and profile-mean pulse-pair correlation and (f) percent spikes per profile and profile-mean pulse-pair
 710 correlation.

725 removing a 1-m along-beam median filtered velocity from each profile (MATLAB's medfilt1, Fig.
 726 A1b). Spikes are flagged as residual velocities which exceed $\pm V_R/2$ (Fig. A1c). It is common
 727 practice with ADCP data to use a minimum allowed correlation to identify bad data. However,
 728 because data spikes in the pulse-coherent ADCP data are driven by the strength of the velocity as
 729 well as the magnitude of the pulse-pair correlation, the pulse-pair correlation of each individual
 730 data point is not a sufficient predictor of individual data quality. Figure A1d shows data probability
 731 density as a function of correlation and the 1-m median filtered velocity. There is a local maximum
 732 in the PDF at V_R and only a weak relationship with correlation. Although the relationship between
 733 velocity and correlation is weak for individual bins, profile-mean correlation is strongly correlated
 734 with the along-beam variance in median-filtered velocity, and thus percent spikes per profile ($R =$

735 0.85, Fig. A1e and Fig. A1f). We flag bad pings using a minimum profile-average correlation
736 value of 50%, and exclude them from further calculations. The resulting quality controlled data is
737 shown in Fig. 2d. In the example burst, 10% of all profiles were flagged as bad.

738 **References**

- 739 Belcher, S., and Coauthors, 2012: A global perspective on Langmuir turbulence in the ocean
740 surface boundary layer. *Geophysical Research Letters*, **39**, L18 605, <https://doi.org/10.1029/2012GL052932>.
- 742 Gargett, A. E., 1999: Velcro measurement of turbulence kinetic energy dissipation rate. *J. Atmos.*
743 *Ocean. Tech.*, **16 (12)**, 1973–1993.
- 744 Gemmrich, J., 2010: Strong turbulence in the wave crest region. *J. Phys. Oceanogr.*, **40**, 583–595,
745 URL DOI:[10.1175/2009JPO4179.1](https://doi.org/10.1175/2009JPO4179.1).
- 746 Gerbi, G., J. Trowbridge, E. Terray, A. J. Plueddemann, and T. Kukulka, 2009: Observations of
747 turbulence in the ocean surface boundary layer: energetics and transport. *J. Phys. Oceanogr.*,
748 **39**, 1077–1096.
- 749 Grare, L., N. Statom, N. Pizzo, and L. Lenain, 2018: Instrumented wave gliders for air-sea
750 interaction and upper ocean research. *Frontiers in marine science*, **B**, <https://doi.org/10.3389/fmars.2021.664728>.
- 752 Hannachi, A., I. Jolliffe, and D. Stephenson, 2007: Empirical orthogonal functions and related
753 techniques in atmospheric science: A review. *International Journal of Climatology*, **27**, 1119–
754 1152, <https://doi.org/10.1002/joc.1499>.
- 756 Hine, R., S. Willcox, G. Hine, and T. Richardson, 2009: The Wave Glider: a wave-powered
757 autonomous marine vehicle. *Oceans*, 1–6, <https://doi.org/10.23919/OCEANS.2009.5422129>.
- 759 Hughes, K., J. Moum, E. Shroyer, and W. Smyth, 2021: Stratified shear instabilities in
760 diurnal warm layers. *Journal of Physical Oceanography*, **51**, 2583–2598, <https://doi.org/10.1175/JPO-D-20-0300.1>.
- 762 Kolmogorov, A. N., 1941: Dissipation of energy in the locally isotropic turbulence. *Dokl. Akad.*
763 *Nauk SSR*, **30**, 301–305.

- 762 Lucas, N. S., J. H. Simpson, T. P. Rippeth, and C. P. Old, 2014: Measuring turbulent dissipation using a tethered adcp. *Journal of Atmospheric and Oceanic Technology*,
763 **31** (8), 1826–1837, <https://doi.org/10.1175/JTECH-D-13-00198.1>, URL <http://dx.doi.org/10.1175/JTECH-D-13-00198.1>.
- 766 McMillan, J. M., A. E. Hay, R. G. Lueck, and F. Wolk, 2016: Rates of dissipation of turbulent
767 kinetic energy in a high reynolds number tidal channel. *Journal of Atmospheric and Oceanic
768 Technology*, **33** (4), 817–837, <https://doi.org/10.1175/JTECH-D-15-0167.1>, URL <http://dx.doi.org/10.1175/JTECH-D-15-0167.1>, <http://dx.doi.org/10.1175/JTECH-D-15-0167.1>.
- 770 Merrifield, M., and R. Guza, 1990: Detecting propagating signals with complex emperical orthogonal
771 functions: a cautionary note. *journal of physical oceanography*, **20**, 1628–1633.
- 772 Mohrholz, V., H. Prandke, and H. Lass, 2008: Estimation of the dissipation rates in dense
773 bottom plumes using a pulse-coherent acoustic doppler profiler (PC-ADCP)- structure function
774 approach. *journal of marine systems*, **70**, 217–239, <https://doi.org/10.1016/j.jmarsys.2007.03.004>.
- 776 Scannell, B. D., T. P. Rippeth, J. H. Simpson, J. A. Polton, and J. E. Hopkins, 2017: Correcting
777 surface wave bias in structure function estimates of turbulent kinetic energy dissipation
778 rate. *Journal of Atmospheric and Oceanic Technology*, **34** (10), 2257–2273, <https://doi.org/10.1175/JTECH-D-17-0059.1>, URL <https://doi.org/10.1175/JTECH-D-17-0059.1>, <https://doi.org/10.1175/JTECH-D-17-0059.1>.
- 781 Shcherbina, A. Y., E. A. D'Asaro, and S. Nylund, 2018: Observing finescale oceanic velocity
782 structure with an autonomous nortek acoustic doppler current profiler. *Journal of Atmospheric
783 and Oceanic Technology*, **35** (2), 411–427, <https://doi.org/10.1175/JTECH-D-17-0108.1>, URL <https://doi.org/10.1175/JTECH-D-17-0108.1>, <https://doi.org/10.1175/JTECH-D-17-0108.1>.
- 785 Sutherland, P., and W. K. Melville, 2015: Field measurements of surface and near-surface turbulence
786 in the presence of breaking waves. *Journal of Physical Oceanography*, **45** (4), 943–965,
787 <https://doi.org/10.1175/JPO-D-14-0133.1>, URL <http://dx.doi.org/10.1175/JPO-D-14-0133.1>.
- 788 Taylor, G. I., 1937: The statistical theory of isotropic turbulence. *J. Aeronaut. Sci.*, **4**, 311.

- 789 Terray, E., M. Donelan, Y. Agrawal, W. Drennan, K. Kahma, A. Williams, P. Hwang, and S. Ki-
790 taigorodskii, 1996: Estimates of kinetic energy dissipation under breaking waves. *J. Phys.*
791 *Oceanogr.*, **26**, 792–807.
- 792 Thomson, J., 2012: Wave breaking dissipation observed with SWIFT drifters. *Journal*
793 *of Atmospheric and Oceanic Technology*, **29** (12), 1866–1882, <https://doi.org/10.1175/JTECH-D-12-00018.1>, URL <https://doi.org/10.1175/JTECH-D-12-00018.1>.
- 795 Thomson, J., J. Girton, R. Jha, and A. Trapani, 2018: Measurements of directional wave spectra and
796 wind stress from a wave glider autonomous surface vehicle. *Journal of Atmospheric and Oceanic*
797 *Technology*, **35**, 347–363, <https://doi.org/https://doi.org/10.1175/JTECH-D-17-0091.1>.
- 798 Thomson, J., M. S. Schwendeman, S. F. Zippel, S. Moghimi, J. Gemmrich, and W. E. Rogers,
799 2016: Wave-breaking turbulence in the ocean surface layer. *Journal of Physical Oceanography*,
800 **46** (6), 1857–1870, <https://doi.org/10.1175/JPO-D-15-0130.1>, URL <http://dx.doi.org/10.1175/JPO-D-15-0130.1>, <http://dx.doi.org/10.1175/JPO-D-15-0130.1>.
- 802 Wiles, P., T. P. Rippeth, J. Simpson, and P. Hendricks, 2006: A novel technique for measuring the
803 rate of turbulent dissipation in the marine environment. *Geophys. Res. Lett.*, **33**, L21 608.
- 804 Zippel, S. F., J. Thomson, and G. Farquharson, 2018: Turbulence from breaking surface
805 waves at a river mouth. *Journal of Physical Oceanography*, **48** (2), 435–453, <https://doi.org/10.1175/JPO-D-17-0122.1>, URL <https://doi.org/10.1175/JPO-D-17-0122.1>, <https://doi.org/10.1175/JPO-D-17-0122.1>.